COMPUTATION OF AIRCRAFT COMPONENT FLOW FIELDS AT TRANSONIC MACH NUMBERS USING A THREE-DIMENSIONAL NAVIER-STOKES ALGORITHM

George D. Shrewsbury, Joseph Vadyak, David M. Schuster, and Marilyn J. Smith
Advanced Flight Sciences Department
Lockheed Aeronautical Systems Company
Marietta, Georgia

INTRODUCTION

A computer analysis has been developed for calculating steady (or unsteady) three-dimensional aircraft component flowfields. This algorithm, called ENS3D, can compute the flowfield for the following configurations: 1) diffuser-duct/ thrust-nozzle, 2) isolated wing, 3) isolated fuselage, 4) wing/fuselage with or without integrated inlet and exhaust, 5) nacelle/ inlet, 6) nacelle (fuselage) afterbody/exhaust-jet, 7) complete transport engine installation, and 8) multicomponent configurations using zonal grid generation techniques.

Solutions can be obtained for subsonic, transonic, supersonic, or hypersonic freestream speeds. The algorithm can solve either the Euler equations for inviscid flow, the thin-shear-layer Navier-Stokes equations for viscous flow, or the full Navier-Stokes equations for viscous flow. The flowfield solution is determined on a body-fitted computational grid. A fully-implicit alternating-direction-implicit method is employed for solution of the finite-difference equations. For viscous computations, either a two-layer eddy-viscosity turbulence model or the k-e two-equation transport model can be used to achieve mathematical closure.

APPROACH

The flowfield solution for a given configuration is determined on a body-fitted three-dimensional curvilinear computational mesh. The computational mesh for each different configuration is determined by a separate grid generation algorithm. Ten grid generation programs are currently used in conjunction with the flow analysis program. Figure 1 illustrates the family of algorithms used to analyze the respective geometry configurations. Most of the existing mesh generation algorithms rely on numerical grid techniques which are based on solving a system of coupled elliptic partial differential equations. Isolated component geometries are typically analyzed using a single block grid approach. Multi-component configurations are typically analyzed using a multi-block H-grid approach where the global computational grid is comprised of a series of cartesian-like sub-grids which are patched together along common interface boundaries.

Once the computational grid is generated, the flowfield is obtained using the ENS3D algorithm by solving either the full three-dimensional Reynolds-averaged Navier-Stokes equations or simplified versions thereof, namely the thin-shear-layer Navier-Stokes equations, or the Euler equations. The thin-shear-layer Navier-Stokes equations retain the viscous and thermal diffusion terms only in the curvilinear coordinate direction normal to the body surface. The retained diffusion terms are generally the most dominant, however, and this approximation allows reduced computer execution times to be achieved without, in many cases, neglecting the most salient viscous flow features. The Euler equations are, of course, applicable to inviscid flow modeling where the vehicle boundary layers remain attached and thin.

The governing equations are cast in strong conservation-law form to admit solutions in which shocks are captured. Second-order differencing is used in computing the metric parameters which map the physical domain to the computational domain. A time-marching fully-implicit approximate factorization scheme is used for solution of the finite-difference equations. Either steady-state or time accurate solutions can be obtained, with second-order or fourth-order spatial accuracy and first- or second-order temporal accuracy. The convective (inviscid) terms in the governing equations are differenced using either central or upwind differencing. The upwind differencing option considers the range of influence and domain of dependence at a solution mesh point, and is used for supersonic flow calculations. The viscous diffusion terms employ central differencing. The algorithm includes the grid speed terms in the contravariant velocity calculations, thereby permitting the computation of unsteady flows with a time-varying grid that can account for elastic deformations of the aircraft structure. Although the interior points are updated implicitly, an explicit boundary condition treatment is employed which allows for the ready adaption of the program to new configurations. To aid convergence, non-reflecting subsonic outflow boundary conditions are employed along with a spatially varying time step for steady-flow solution cases. For the central difference option, the algorithm can use either a constant coefficient artificial dissipation model or a variable coefficient model where the coefficient's magnitude is based on the local pressure gradient. For the upwind differencing option, the algorithm is naturally dissipative. Laminar viscosity is computed for viscous cases using Sutherland's law. For turbulent viscous flows, the effective eddy viscosity is currently computed using either the Baldwin-Lomax two-layer algebraic turbulence model or the k-e two-equation transport model. For cases with separation, a streamwise eddy viscosity relaxation scheme is also used in conjunction with the Baldwin-Lomax turbulence model. This accounts for turbulence history effects and improves the simulation of separated flowfields.

In an effort to reduce the required computer execution time, versions of the flow simulation algorithm were developed for use on Class VI vector supercomputers. The ENS3DC version was written for the CDC CYBER-205 and employs a fully vectorized block tridiagonal simultaneous equation solution scheme and vectorized coefficient calculations to improve algorithm efficiency. ENS3DV is a similar version written for a Lockheed CRAY X-MP/24 using one of two central processors available on this machine. ENS3DVM is a modified version of ENS3DV which employs the multitasking process to operate both of the central processors available on the CRAY X-MP/24 simultaneously on the same source code. The use of these vectorized versions has dramatically reduced the required execution time. For instance, the ENS3DV version is about 10 times as fast as the ENS3D version when measuring CPU time on a single processor of the CRAY X-MP/24. The ENS3DVM version yields a factor of approximately 2 improvement in speed over the ENS3DV version when measuring wall clock execution time in a dedicated environment on the CRAY X-MP/24. Additional versions of the program exist for performing flowfield calculations at hypersonic Mach numbers. These versions account for real gas effects by using parametric curve fits to calculate pressure, temperature, and sonic speed as function of density and internal energy for equilibrium air. Another version of the program solves a system of species continuity equations in addition to the five mean flow equations and thereby permits flowfield calculations with finite-rate thermochemical effects. This version is used to model H2 – air combustion flows for hypersonic cruise vehicles. Applications of the ENS3D algorithm are presented in reference 1.

SAMPLE RESULTS

Correlation studies have been performed for all of the computational options. These studies are documented in References 1,2,3,4,5, and 6. Selected results are presented below to illustrate application of the analysis.

Afterbody/ Exhaust-Jet Flow Simulations

The AGRID and ENS3D algorithms were used in performing correlation studies for afterbody/exhaust-jet configurations. The AGRID algorithm can generate the three-dimensional body-fitted grid for arbitrary nacelle (fuselage)/ exhaust-jet configurations. The grid is obtained using two-dimensional grid generation techniques for a series of meridional planes splayed circumferentially around the body. The AGRID and ENS3D algorithms are capable of simulating the flowfield for: (1) afterbody/plume-simulator, (2) turbojet (single exhaust jet), and (3) turbofan (coaxial exhaust jet) configurations at arbitrary speed and incidence.

Turbulent Thin-Shear-Layer

Navier-Stokes computations were performed for an afterbody/plume-simulator configuration for free-stream Mach numbers M_∞ of 0.4 and 0.9, zero incidence ($\alpha = 0^\circ$), and Reynolds numbers Re of 1,300,000 and 1,900,000, respectively. This configuration was tested by Reubush (reference 7) at NASA-Langley and has a circular arc afterbody contour with a fineness ratio (ratio of afterbody length to maximum afterbody diameter) of 2.0 and a closure ratio (ratio of nozzle exit diameter to maximum afterbody diameter) of 0.7. Figure 2 illustrates the computed surface pressure coefficient Cp plotted as a function of the nondimensional distance X/dm (distance/afterbody diameter) measured along the afterbody. Also shown are the corresponding experimental data (reference 7). These results correspond to an attached flow case.

Figure 3 illustrates the computed pressure distribution for another afterbody/ plume-simulator configuration for a free-stream Mach number M_∞ of 0.9, zero incidence ($\alpha = 0^\circ$), and a turbulent flow Reynolds number of 1,900,000. These results correspond to a shock-induced separated flow case and are for an afterbody with a fineness ratio of 1.0 and a closure ratio of 0.5. Also shown in the figure are the corresponding experimental data (reference 7). Good agreement is observed between the results of the analysis and experiment. This calculation required using eddy viscosity relaxation in conjunction with the Baldwin-Lomax turbulence model.

Figure 4 illustrates the computed surface pressure distribution for a turbojet afterbody with $M_\infty = 0.9$, $\alpha = 0^\circ$, and Re = 1,900,000. Uniform jet inflow conditions with a turbulent nozzle wall boundary layer velocity profile were specified. The jet inflow conditions correspond to a jet total to free-stream static pressure ratio of 2.0. Also shown along with the results of the turbulent thin-shear-layer Navier-Stokes calculations are the corresponding experimental data (reference 8).

Turbofan Engine Installation Flow Simulations

The NGRID, AGRID, and ENS3D algorithms were used in performing flow simulations for complete turbofan engine installations. The NGRID algorithm can generate the three-dimensional body-fitted grid for arbitrary nacelle/inlet forebody configurations. Like AGRID, NGRID generates the nacelle forebody grid by using two-dimensional grid generation techniques for a series of meridional

planes arranged around the body. The NGRID and AGRID codes can be linked together to generate grids for complete engine installations.

Flow computations (reference 2) have been performed for an asymmetric turbofan engine installation. The configuration under study is a recent Lockheed drooped-inlet design in which the inlet contour has circumferential variation both in section shape and in length from the hilite point to the compressor face. The front of the inlet is tilted downward with respect to the engine centerline for the purpose of aligning the inlet with the local flow direction underneath the wing. Figure 5 illustrates the engine installation contours, and a portion of the computational meridional plane grid for the top ($\theta = 0^\circ$) circumferential station (upper symmetry meridian). The nacelle has one plane of geometric symmetry. The configuration has an asymmetric circular arc afterbody contour for the outer (fan) cowl. The contour around the primary (gas generator) nozzle is also a circular arc but is axisymmetric. Turbulent flow calculations have been performed for the turbofan engine configuration illustrated in Figure 5. Figure 6 presents the symmetry plane velocity vector field for a turbulent thin-shear-layer Navier-Stokes calculation. The flow conditions correspond to a free-stream Mach number of 0.8, an angle of attack of 0°, an effective compressor face Mach number MCF of 0.35, Reynolds number Re of 2,400,000/ft, a primary jet Mach exit number MJP of 1.0, and a fan jet Mach exit number MJF of 1.0. The mixing layers between the primary jet and fan jet, and fan jet and external flow are illustrated in the figure. The exhaust jet velocity profiles were specified to be in the axial direction and were composed of a uniform jet core velocity profile and a turbulent boundary layer velocity profile next to a given solid surface.

For an asymmetric nacelle, the flow will be three-dimensional even at zero incidence. Computed surface pressure distributions for the top ($\theta = 0^\circ$) and bottom ($\theta = 180^\circ$) meridians of the asymmetric engine installation are presented in Figure 7. Asymmetry exists in the computed solution with the lower external surface producing a higher suction level than the top meridian at this angle of attack. Transition was specified as occurring at the suction peak.

Transport Wing Flow Simulations

The WGRID and ENS3D algorithms were used in performing correlation studies for isolated wing configurations. The WGRID code can generate the three-dimensional, body-fitted grid for wings with arbitrary planforms and section shapes. The computational mesh is obtained using two-dimensional, numerical, grid-generation techniques for a series of spanwise stations that are arranged along the span. An option exists within the WGRID and ENS3D algorithms to compute the flowfield for a wing contained between two parallel walls. Either an O-grid or C-grid topology can be used in analyzing isolated wing flowfields.

Flow computations, both inviscid Euler and viscous thin-shear-layer Navier-Stokes, have been performed for the Onera M-6 swept and tapered wing (reference 9). Figure 8a illustrates the wing section and the spanwise plane C-grid used in performing the Euler computations. The grid used for viscous computations has finer mesh spacing in the normal direction and had an increased number of normal stations.

Figure 8b compares Onera M-6 wing experimental data and the results of the ENS3D algorithm executed in the Euler equation mode for $M_\infty = 0.84$, and $\alpha = 0^\circ$. Correlation results were determined for a number of semispan locations. The analysis and experimental data semispan locations are denoted by η_{th} and η_{exp},

respectively. Except for a slight under-prediction of the suction peak, good agreement was obtained.

Figure 8c presents additional correlations between the analysis executed in the thin-shear-layer Navier-Stokes mode and experimental data for M_∞ = 0.7, α = 1°, and Re = 11,740,000. This calculation used the finer grid and a fully turbulent flow approximation. Again, except for under-prediction of the suction peak, good agreement was obtained.

<div align="center">Advanced Transport Vehicle and Generic Fighter Simulations</div>

The WGRID, WBGRID, and ENS3D algorithms were used in performing simulations for an advanced transport vehicle and a high technology generic fighter configuration. The WBGRID code is able to generate the grid for a variety of wing/fuselage configurations. The mesh is obtained using two-dimensional numerical grid generation techniques for the symmetry and freestream sidewall planes and three-dimensional numerical grid generation techniques for stations in between these spanwise stations.

Viscous flow simulations have been performed for a blended wing-body advanced transport vehicle configuration. Figure 9a presents the surface grid for this vehicle. The wing is swept and tapered. The fuselage section ordinates were obtained by linearly interpolating between those on the symmetry plane and those at the wing break. Figure 9a also shows a portion of the spanwise plane field C-grid near the wing break.

Thin-layer Navier-Stokes computations were performed for this configuration for M_∞ = 0.8, α = 0°, and Re = 4×10^6. A fully turbulent flow approximation was used in the analysis.

Figure 9b presents the computed surface static pressure field for this vehicle. The highest pressure is denoted by red and the lowest is denoted by blue. The highest pressure is at the vehicle's nose and at the wing's leading edge, whereas maximum suction occurs near mid-chord on the wing. This figure also shows the field pressure distribution on a portion of a spanwise station near the wing break.

Figure 9c presents the computed surface pressure coefficient Cp plotted as a function of fractional chord x/c for the 7.07% (η = .07) and 60.0% (η = .60) semispan locations. The vehicle is designed to have nearly shock-free compressions. Greater loading occurs on the wing than on the fuselage, although the fuselage does contribute to the total lift of the vehicle.

Thin-layer and full Navier-Stokes viscous flow simulations have been performed for a Lockheed generic fighter configuration. Figure 10a illustrates this vehicle along with the grid used in the computations. The vehicle has a straked forebody with a sharp leading edge. The wing has biconvex airfoil sections of low thickness with sharp leading edges.

Figure 10b illustrates the computed pressure distribution for a thin-layer Navier-Stokes calculation at M_∞ = 0.8, a = 1°, and Re = 4×10^6. Again, a fully turbulent flow approximation was used. This figure presents the computed surface pressure coefficient Cp as a function of fractional chord x/c for the 6 percent (η = 0.06) and 72 percent (η = 0.72) semispan locations. The η = 0.06 station corresponds to the fuselage. Compression occurs at the leading edge with a double peak expansion occurring on the fuselage's upper surface. An engine pod assembly was attached to the vehicle's lower side which gives rise to

an expansion and subsequent recompression around the pod as shown in the figure. The $\eta = 0.72$ location corresponds to a wing station.

Hypersonic Cruise Vehicle with Power Addition Effect Simulations

The ENS3D algorithm has also been employed to analyze hypersonic cruise vehicles with power addition effects at subsonic, transonic, supersonic, and hypersonic Mach numbers. One of the major concerns associated with hypersonic vehicles operating in the transonic range is the prediction of the complex afterbody flowfields associated with the hypersonic airframe/propulsion integration problem. The majority of hypersonic vehicle designs use a highly upswept afterbody as a nozzle surface for operation at hypersonic conditions. The afterbody is designed so that the propulsion system exhaust plume expands into the upswept afterbody creating an efficient nozzle system. At transonic speeds however, the exhaust plume does not fill this region and the flow separates. This results in increased drag and pitching moment changes which can severely impact the performance of the vehicle as it accelerates to hypersonic flight. Therefore, accurate computational aerodynamics methods are required to predict these flows, thus enabling the aerodynamicist to evaluate and modify the design in a timely and cost-effective manner.

The configuration investigated employed an upswept conical afterbody with a semi-circular exhaust nozzle. This design is representative of a number of scramjet installations currently under consideration for hypersonic cruise vehicles. The configuration forebody was effectively uncambered to eliminate any pressure gradients leading up to the nozzle exit. The wing design was a symmetrical bi-convex airfoil section and the planform was designed to shield the afterbody from the upper surface flow. A computer rendition of this configuration is shown in Figure 11.

A single-block fuselage grid topology was chosen to model the hypersonic configuration. The topology was modified at the wing trailing edge to allow grid lines on the wing surface to leave the trailing edge onto a wake surface rather than abruptly collapsing to the symmetry plane. This eliminates problems with grid skewness at the wing trailing edge, but forces the user to model the upper and lower halves of the geometry with the same number of spanwise points.

Figure 12 shows an isometric view of the surface grid. Two axial grid planes have been added to this figure to show the circumferential grid topology used to model the geometry and the general distribution of the flowfield grid points. This grid consists of 82 points in the streamwise direction, 42 points circumferentially and 27 points normal to the body surface. This gives a total of approximately 93,000 total points which requires 3.4 million words of storage in the ENS3D algorithm. ENS3D is run on Lockheed's Cray X-MP/24 and this grid size is very close to the limit which can be run on this computer.

Figure 13 shows a side view of the surface grid with the upper and lower symmetry plane grids added. This view shows the streamwise grid topology and the axial distribution of grid points. Axial stations have been clustered in the jet/afterbody region which is the primary zone of interest in this study. This sacrifices resolution on the forebody, but since only the overall effect of the forebody on the afterbody flow is desired, this grid density is sufficient to capture the required flowfield qualities. The figure also shows that the jet exit has been modeled as a slanted surface rather than a vertical exhaust plane. This was done so as to eliminate abrupt changes in the grid metrics which could cause convergence problems in ENS3D.

ENS3D computations were conducted for this configuration at a $M_\infty = 0.7$, $\alpha = 0^\circ$, Re = 7,000,000, and a jet pressure ratio of 2.0, which corresponds to a choked jet. Figure 14 shows a color Mach number contour of an ENS3D solution on the model afterbody at the centerline. The figure clearly shows that the flow has separated from the afterbody and the deflection of the jet behind the vehicle is also shown. Figure 15 shows the Mach number contour on a transverse cut through the afterbody. This figure shows that the maximum Mach number is not attained on the vehicle centerline, but rather near the wing/body intersection, thus indicating the highly three-dimensional nature of this flowfield.

COMPUTER RESOURCE REQUIREMENTS

The ENS3D flow simulation algorithm is best suited for execution on Class-VI vector supercomputers. A vectorized version (ENS3DV) and a vectorized/multitasked version (ENS3DVM) are the most efficient versions of the algorithm and were written for use on the CRAY X-MP and CRAY-2 computer systems. The multitasked ENS3DVM version reduces the wall clock execution time required by the ENS3DV version by a factor approximately equal to the number of central processors available on the machine if the program is executed in a dedicated environment. Although the wall clock execution time is reduced using the multitasked ENS3DVM version, the total CPU time remains approximately the same as using the single processor ENS3DV version since multitasking simply splits the computational work load over a number of processors. The machine billing algorithm generally uses the total CPU time and allocated memory in determining the cost of a given execution.

The execution speed of the ENS3DV version of the algorithm is problem dependent. Two primary vector lengths are incorporated into the algorithm: (1) the number of wraparound or axial grid stations (Im), and (2) the number of block tridiagonal inversions to be performed simultaneously (N_I). For a fixed total grid size and fixed number of time steps, increasing Im and/or N_I will reduce the required execution time. This is because on all vector computers increasing the vector length reduces the number of internal clock periods per result, thereby increasing execution speed. The effect of increasing N_I while fixing the grid size and number of time steps is illustrated for a sample problem in Figure 16. The problem under study is the solution of a steady viscous turbulent flowfield for a sample configuration. A grid size of approximately 40,000 points was employed and 800 time steps were used in the execution to achieve a converged solution. At the same time, a spatially variable time step was used to accelerate convergence. Shown in the figure are single central processor execution times as a function of N_I for both turbulent thin-shear-layer and turbulent full Navier-Stokes executions. In all cases, increasing N_I reduces the required CPU time. Increasing N_I, however, increases the amount of temporary storage. The product of storage and execution time can increase with higher vector lengths to actually increase the number of system billing units (SBU) which is a measure of the total job cost. The results presented in Figure 16 are for a Lockheed CRAY X-MP/24 computer. Billing algorithms can be site dependent and may weight processor time and memory differently.

The ENS3DV algorithm requires a memory allocation of roughly 34 times the number of computational grid points plus some temporary storage overhead, which increases as does N_I, as described previously.

CONCLUSIONS

An analysis has been presented for calculating the flowfield for a variety of aircraft components. Solutions have been obtained by solving the viscous

Navier-Stokes equations on body-fitted curvilinear grids using a fully-implicit approximate factorization algorithm. Enhancements currently being incorporated into the algorithm include: discrete bow shock wave fitting, upwind differencing for supersonic flow calculations, a solution adaptive grid scheme, and turbulent viscosity field calculation using a transport equation model.

REFERENCES

1. Vadyak, J., Smith, M. J., Schuster, D. M., Shrewsbury, G. D., "Simulation of Aircraft Component Flowfields Using a Three-Dimensional Navier-Stokes Algorithm," 3rd Cray International Science and Engineering Symposium, Cray Research, Inc., Minneapolis, Minnesota, September, 1987.

2. Vadyak, J., "Simulation of Nacelle-Afterbody/Exhaust-Jet Flowfields Using a Three-Dimensional Navier-Stokes Algorithm," AIAA Paper No. 85-1283, July, 1985.

3. Vadyak, J. and Smith, M. J., "Simulation of Engine Installation Flowfields Using a Three-Dimensional Euler/Navier-Stokes Algorithm," AIAA Paper No. 86-1537, June, 1986.

4. Vadyak, J., "Simulation of Transonic Three-Dimensional Nacelle/Inlet Flowfields Using an Euler/Navier-Stokes Algorithm," AIAA Paper No. 85-0084, January, 1985.

5. Vadyak, J., "Simulation of Diffuser Duct Flowfields Using a Three-Dimensional Euler/Navier-Stokes Algorithm," AIAA Paper No. 86-0310, January, 1986.

6. Vadyak, J., Smith, M. J., Schuster, D. M., and Weed, R., "Simulation of External Flowfields Using a 3-D Euler/Navier-Stokes Algorithm," AIAA Paper No. 87-0484, January 1987.

7. Reubush, D. E., "Experimental Study of the Effectiveness of Cylindrical Plume Simulators for Predicting Jet-On Boattail Drag at Mach Numbers up to 1.3," NASA TN D-7795, 1974.

8. Reubush, D. E., and Runckel, J. F., "Effect of Fineness Ratio on Boattail Drag of Circular-Arc Afterbodies having Closure Ratios of 0.50 with Jet Exhaust at Mach Numbers up to 1.30," NASA TN D-7192, 1973.

9. Schmitt, V., and Charpin, F., "Pressure Distribution on the Onera M-6 Wing at Transonic Mach Numbers," AGARD-AR-138, 1979.
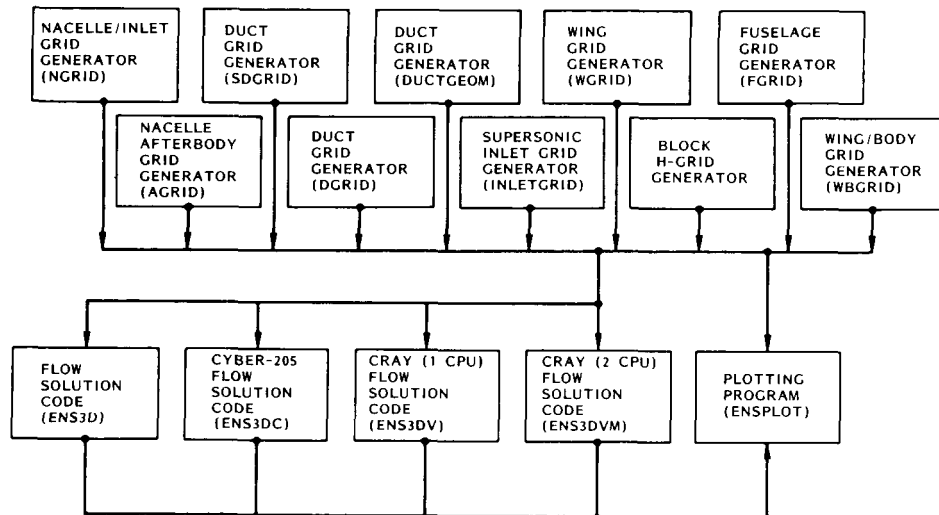
Figure 1. Family of 3-D Flow Analysis Algorithms

AFTERBODY/PLUME-SIMULATOR
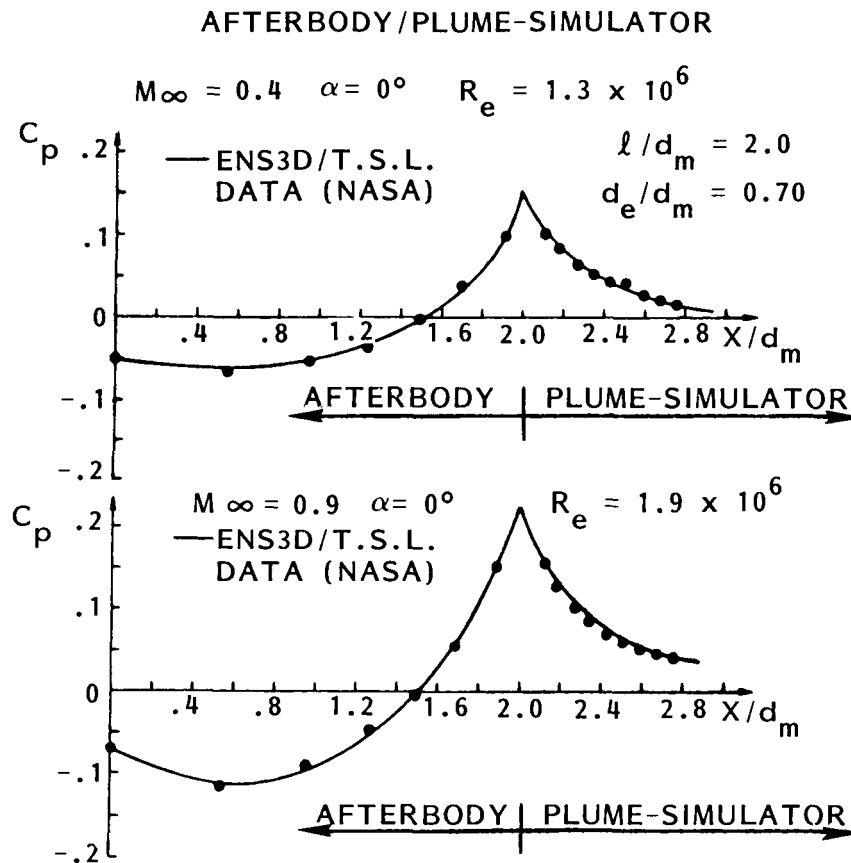
Figure 2. Afterbody/Plume-Simulator Pressure Distributions (Attached Flow)

183
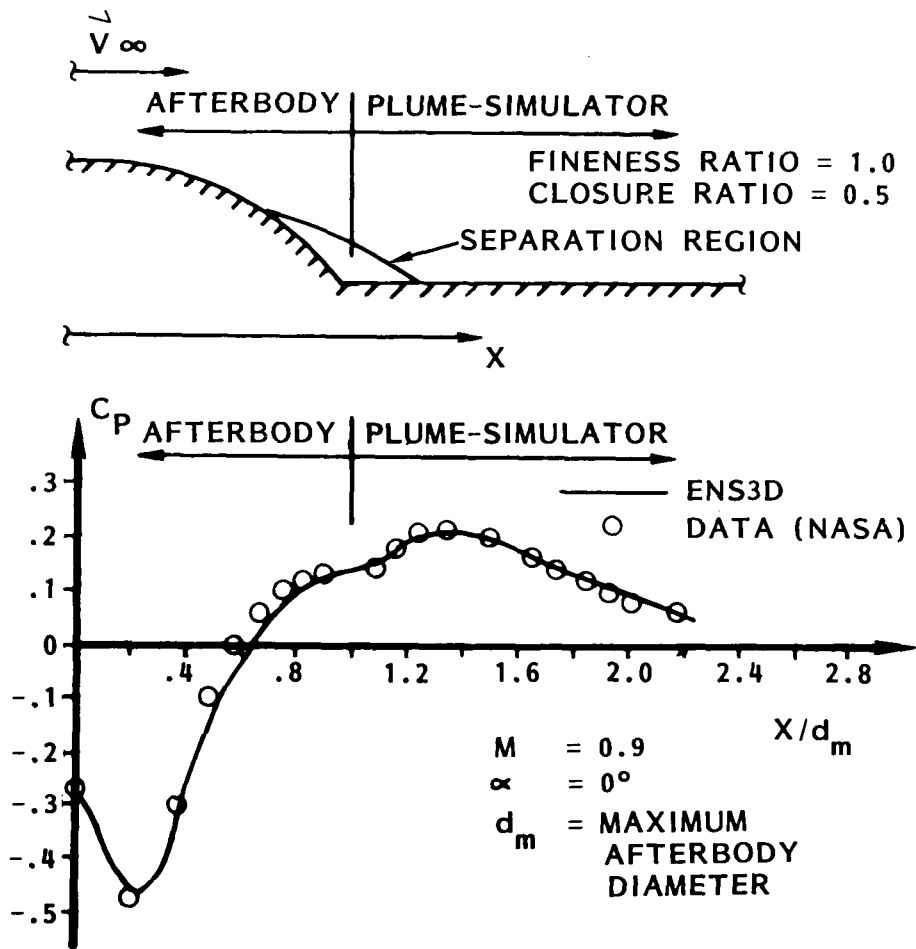
Figure 3. Afterbody/Plume-Simulator Pressure Distribution (Separated flow)
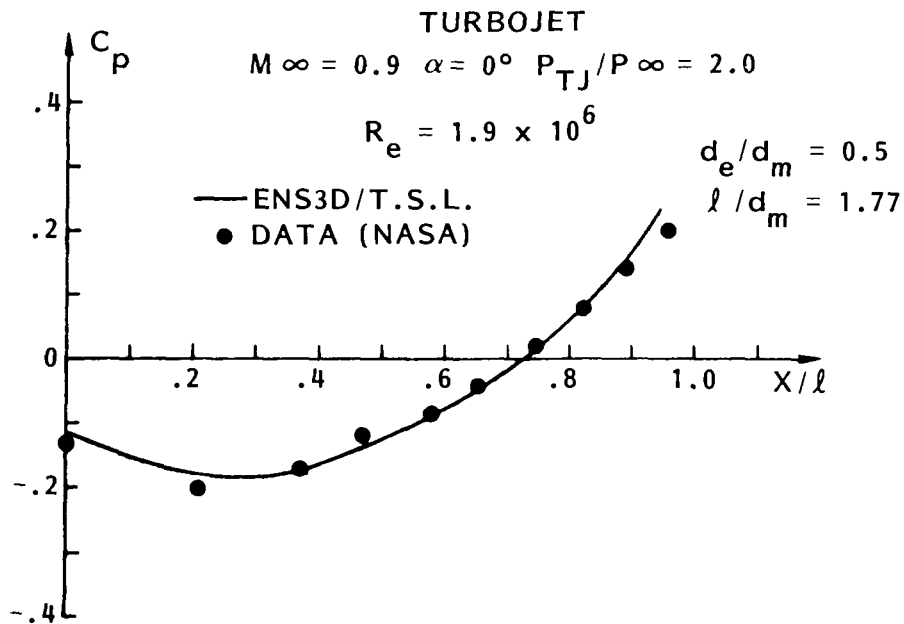
Figure 4. Turbojet Afterbody Pressure Distribution
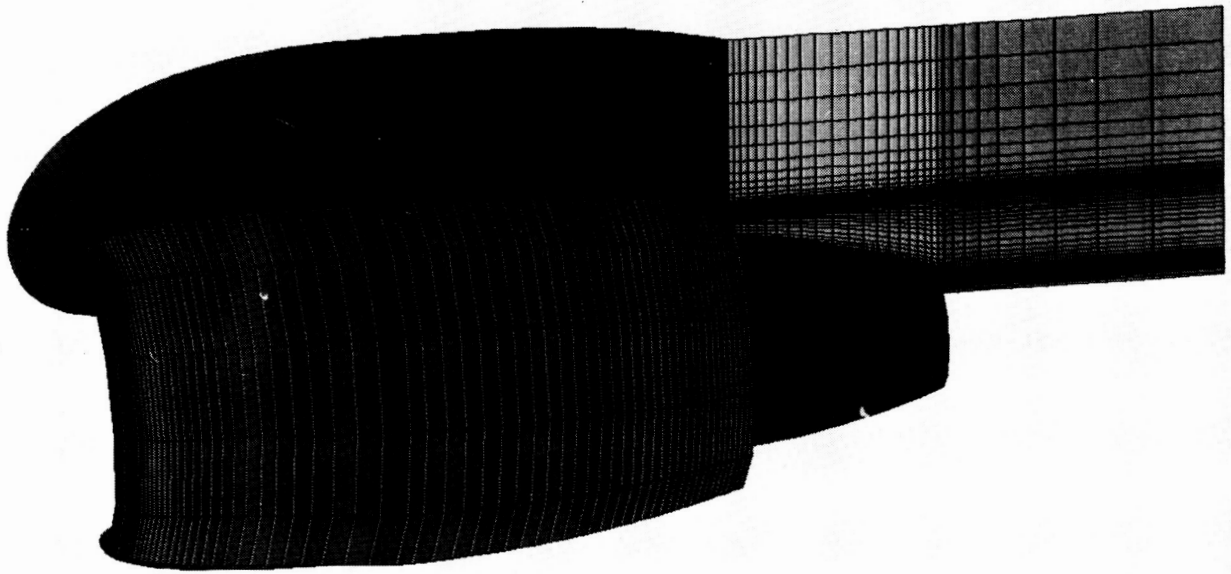
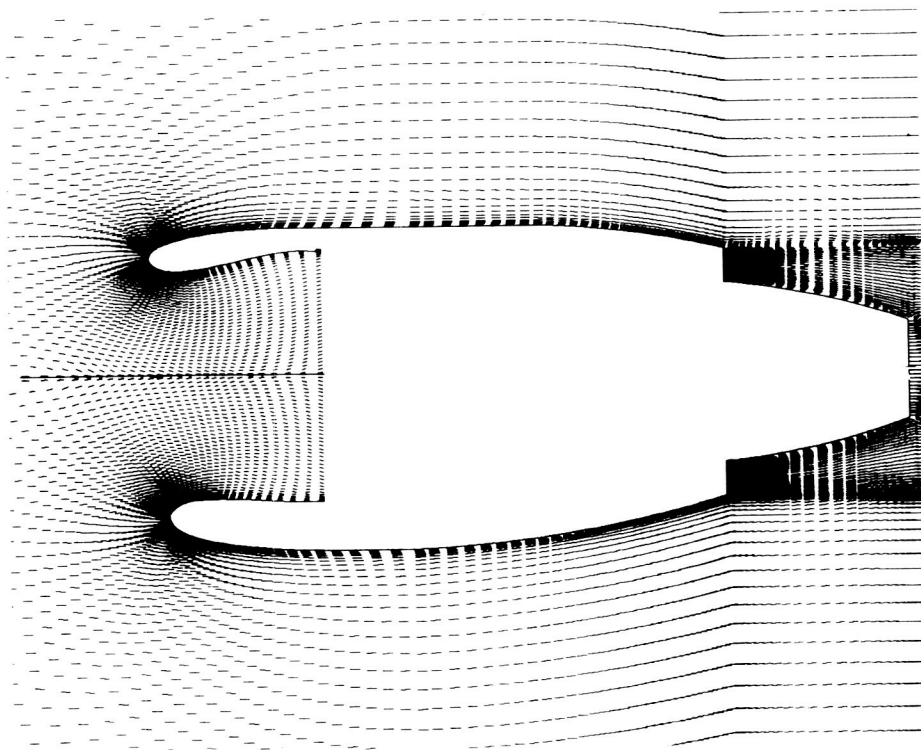ENGINE ZONAL GRID
ELEV= 20.00 YAW= 80.00

Figure 5.   Turbofan Engine Grid
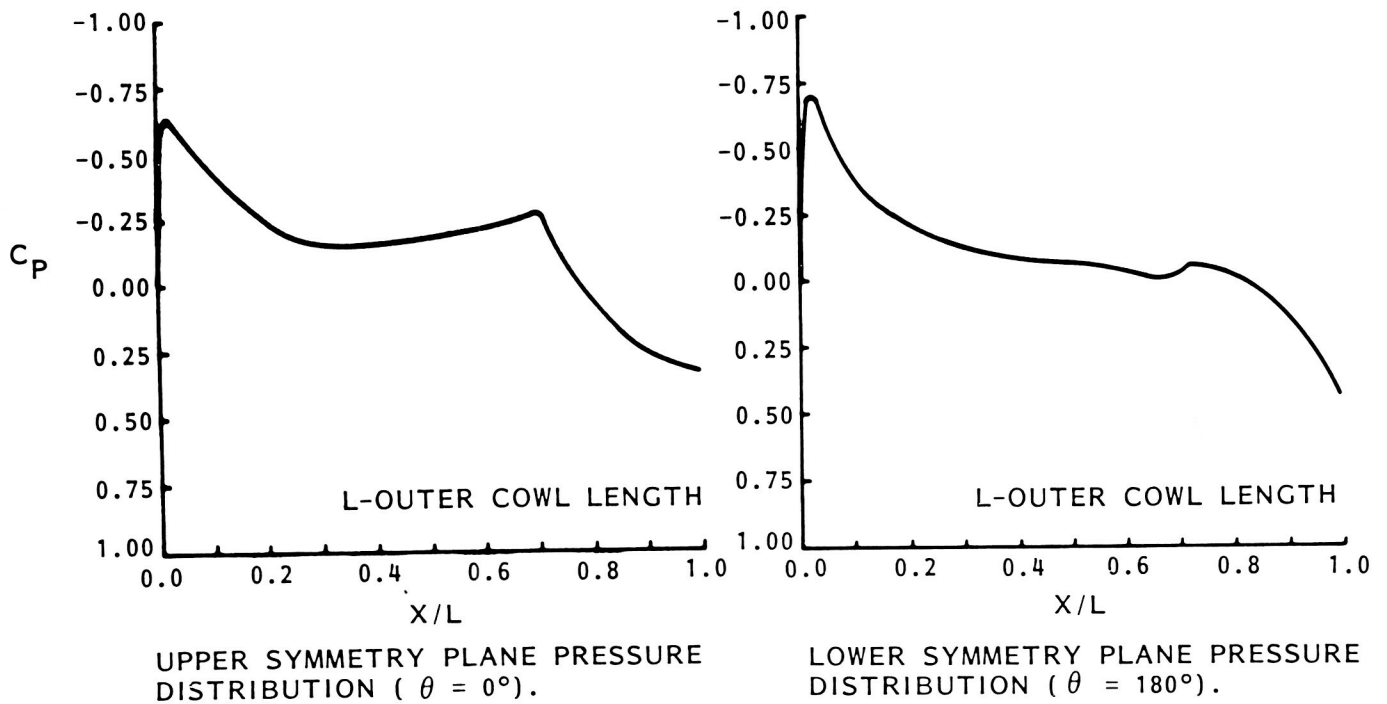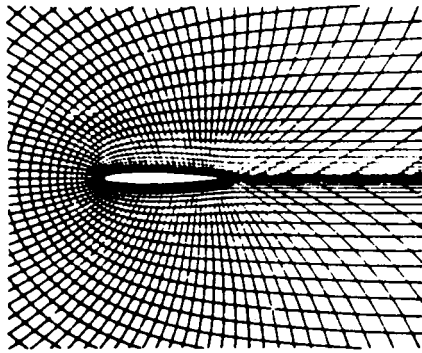
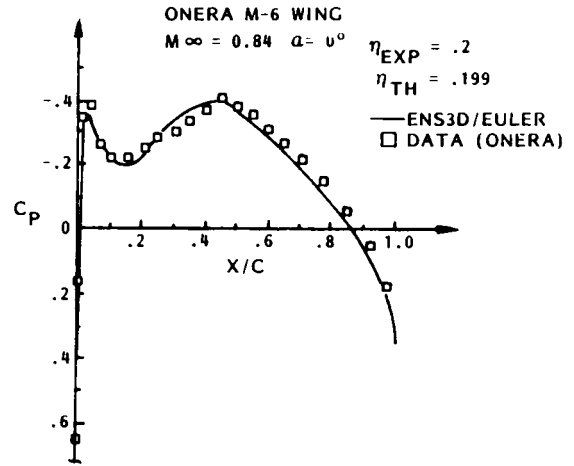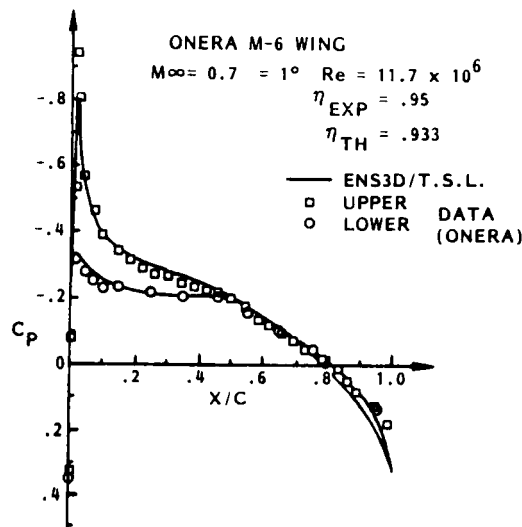Figure 6. Turbofan Engine Symmetry Plane Velocity Vectors

UPPER SYMMETRY PLANE PRESSURE
DISTRIBUTION (θ = 0°).

LOWER SYMMETRY PLANE PRESSURE
DISTRIBUTION (θ = 180°).

Figure 7. Turbofan Engine Pressure Distributions

186

(a) SPANWISE PLANE GRID.

(b) PRESSURE DISTRIBUTION FOR EULER SOLUTION.

(c) PRESSURE DISTRIBUTION FOR THIN-SHEAR-LAYER NAVIER-STOKES SOLUTION.

Figure 8. Grid and Pressure Distribution for Onera M-6 Wing

SPANWISE
PLANE
GRID
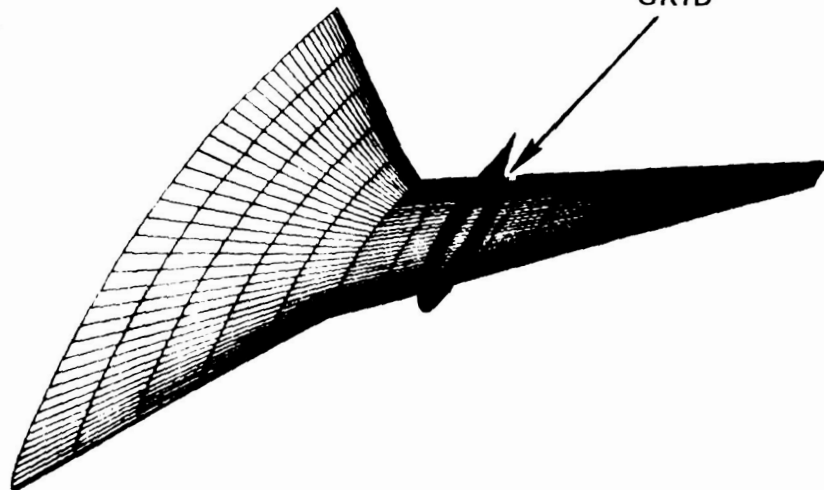
a.)   Surface Grid for Advanced Transport
Vehicle

ATT
MACH= 0.80 ALPHA=   0.00
0.50   0.61   0.72   0.84   0.95
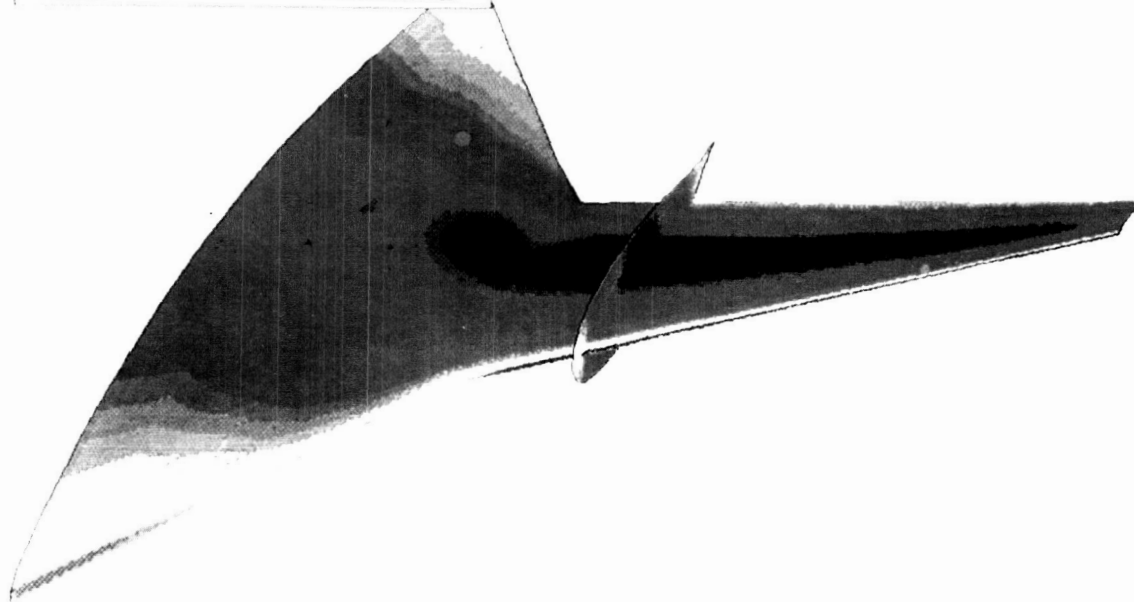
b.)   Surface Pressure Distribution for Advanced Transport.

Figure 9.   Grid and Pressure Distribution for Advanced Transport
Vehicle

DISTRIBUTION AT 7.0% SEMISPAN STATION   DISTRIBUTION AT 60% SEMISPAN STATION
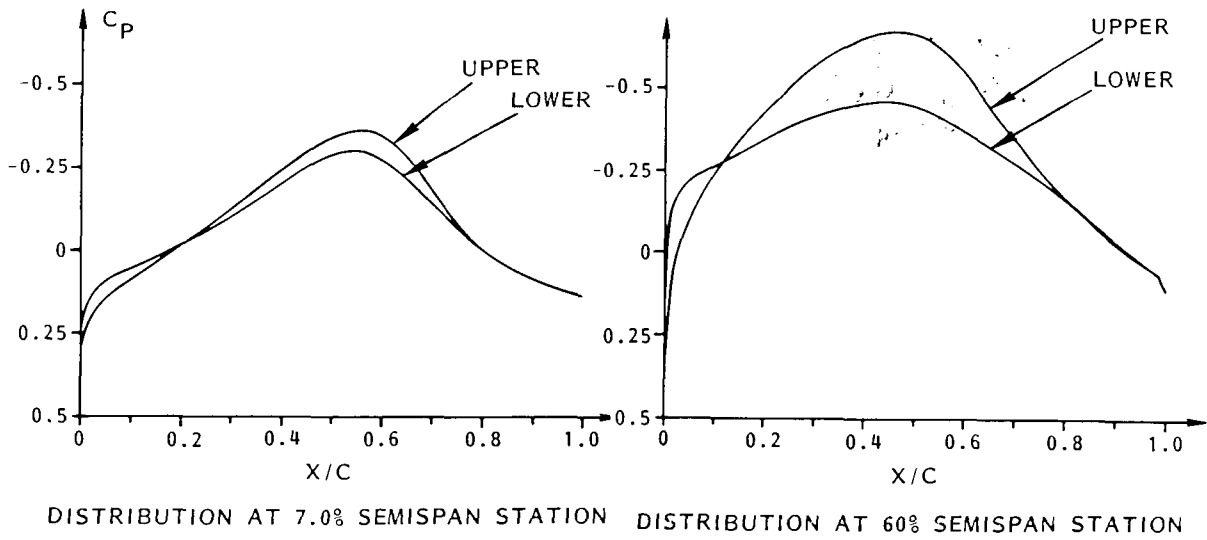
c) Surface Pressure Coefficient
Distribution for Advanced Transport at
$M_\infty = 0.8$ and $\alpha = 0°$.

Figure 9.   Grid and Pressure Distribution for Advanced Transport
Vehicle

GENERIC FIGHTER
ELEV= 50.00 YAW= 10.00

a.   Surface Grid.

DISTRIBUTION AT 6% SEMISPAN STATION   DISTRIBUTION AT 72% SEMISPAN STATION
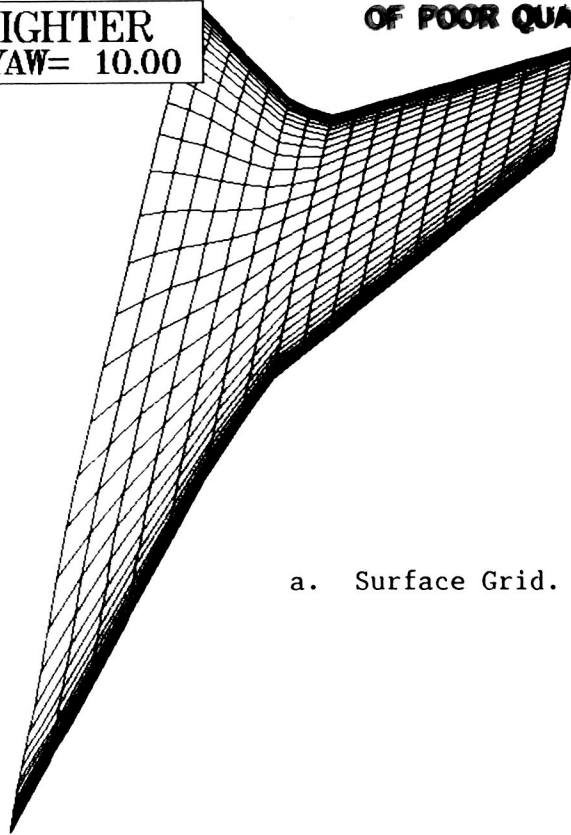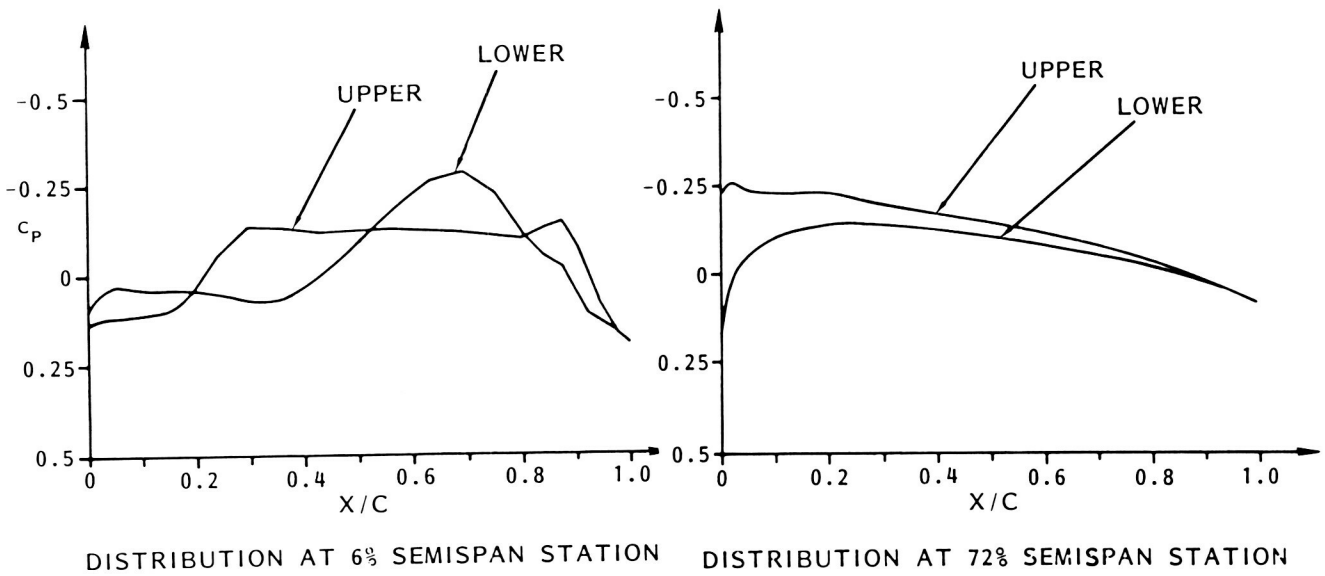
b.   Surface Pressure Coefficient distribution for
     $M\infty$ = 0.8 and α = 1°.

Figure 10.   Grid, Pressure Distribution, and Velocity Field for
             Advanced Fighter

Figure 11.   Generic Hypersonic Configuration

HYPERSONIC MODEL
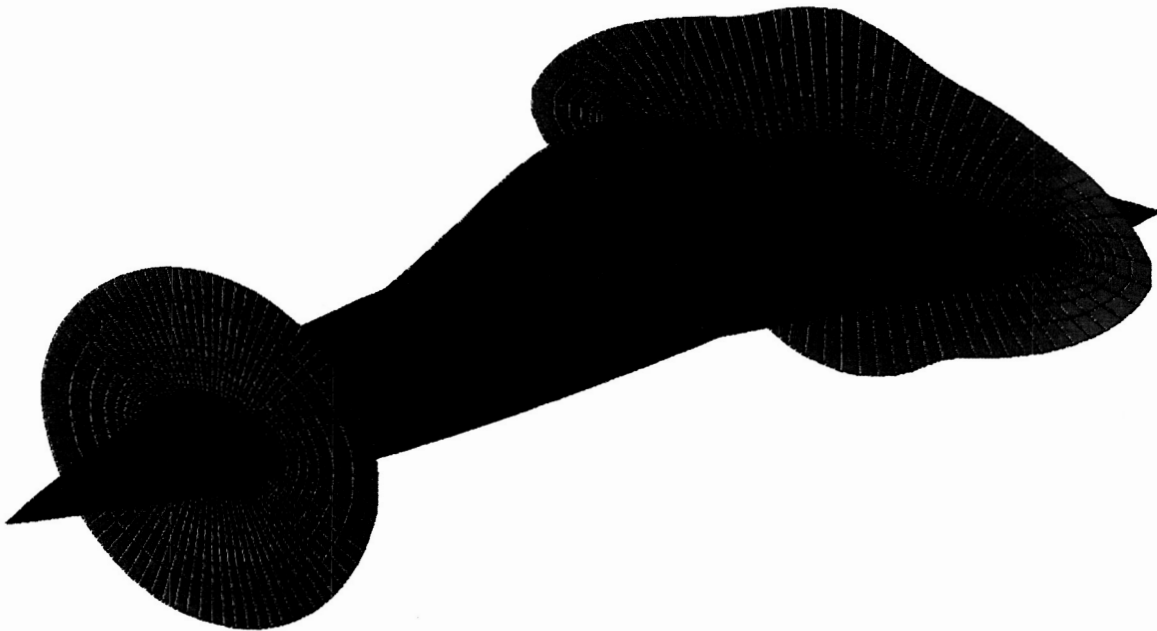
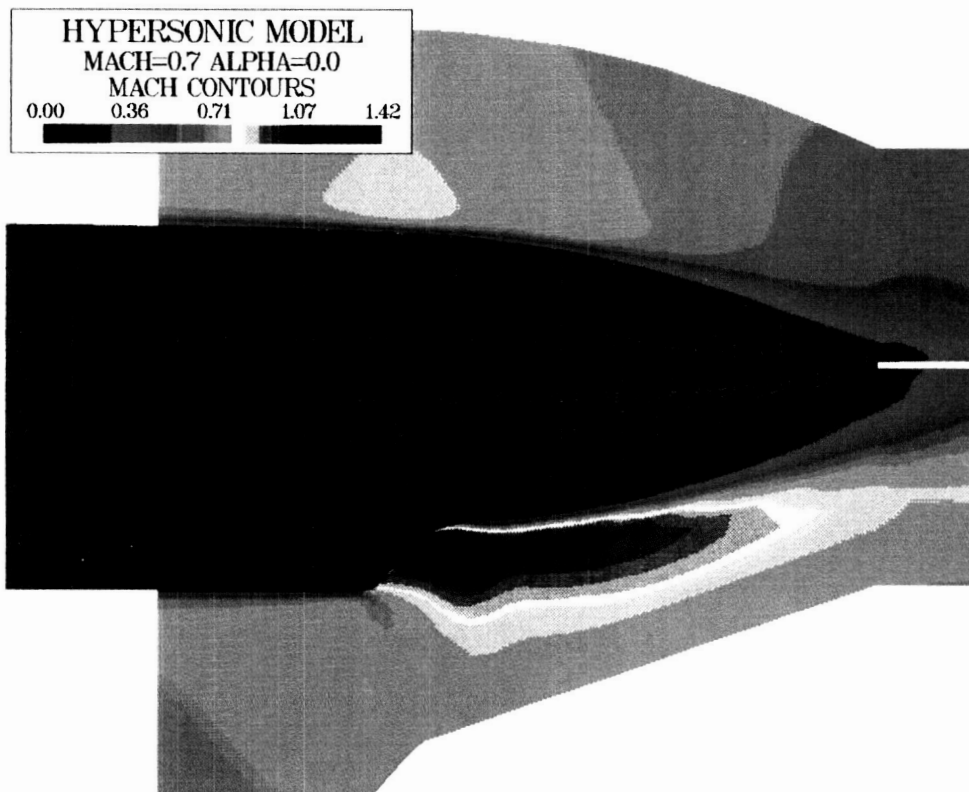Figure 12.   Surface and Circumferential Grids
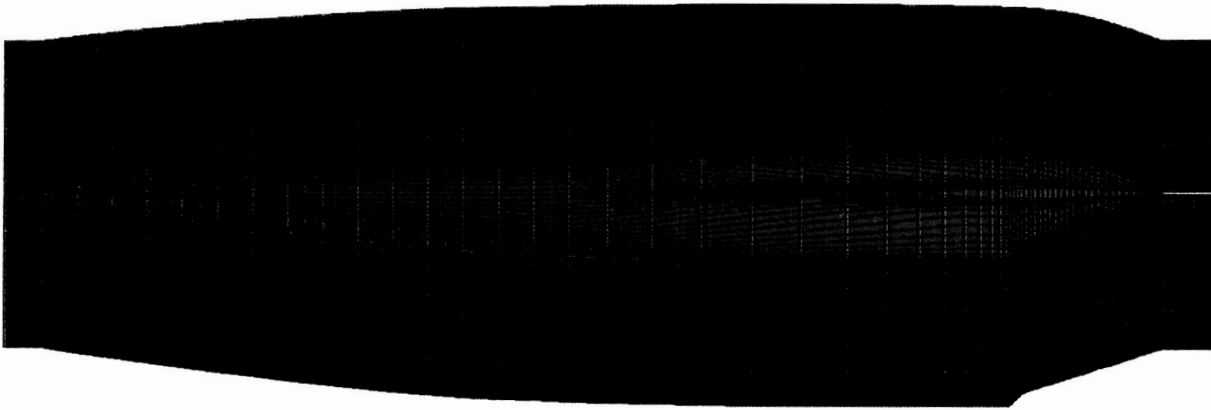
Figure 13. Symmetry Plane Grid

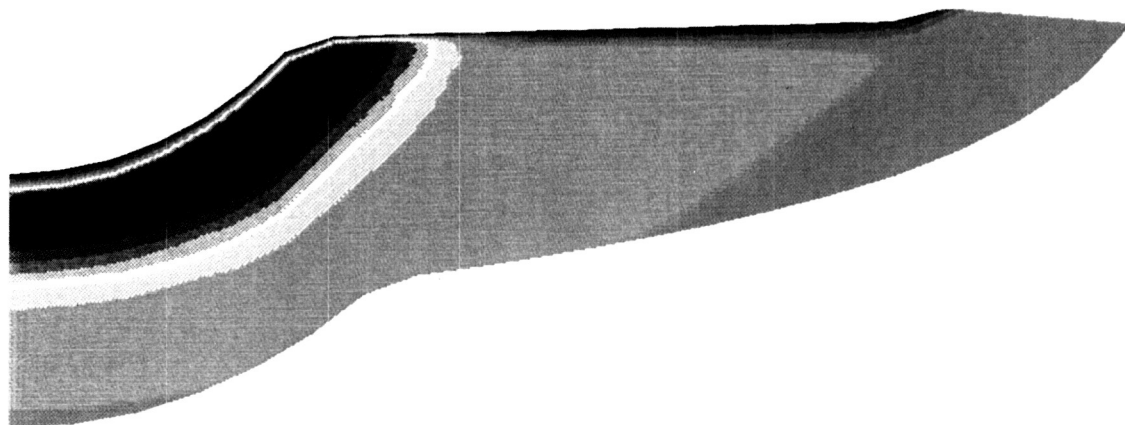Figure 14. Mach Number Contours on 20 Degrees Upswept Afterbody, NPR 2.0

HYPERSONIC MODEL
MACH=0.7 ALPHA=0.0
MACH CONTOURS
0.00   0.37   0.75   1.12   1.50
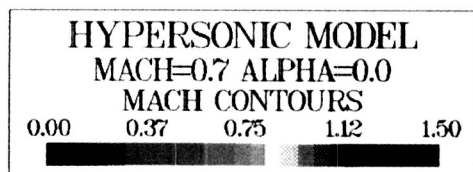
Figure 15.   Spanwise Mach Number Contour in Jet/Afterbody Region, NPR 2.0
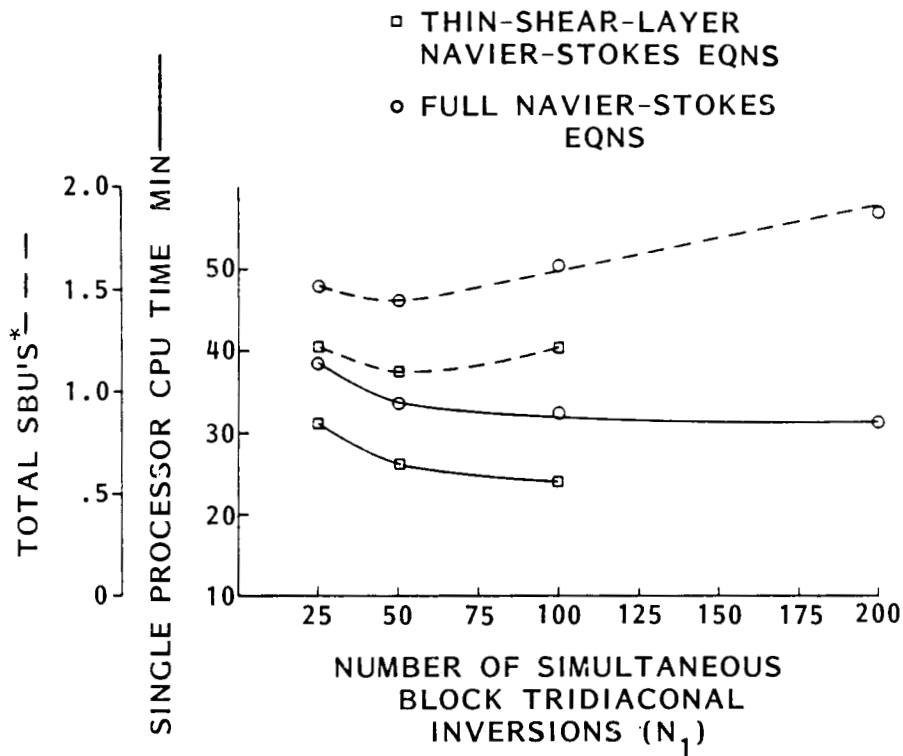
Figure 16. ENS3DV (Single Processor) CRAY CPU Time and SBU Usage as a Function of Number of Simultaneous Inversions [CFT 1.14 Compiler on CRAY X-MP/24]